



# INCORPORATION OF Mo<sup>6+</sup> IN FERRIHYDRITE, GOETHITE, AND HEMATITE

MARCEL G. GÖRN<sup>1,\*</sup>, RALPH M. BOLANZ<sup>1</sup>, STEPHEN PARRY<sup>2</sup>, JÖRG GÖTTLICHER<sup>3</sup>,  
RALPH STEININGER<sup>3</sup>, AND JURAJ MAJZLAN<sup>1</sup>

<sup>1</sup>Institute of Geosciences, Friedrich-Schiller-University Jena, 07745 Jena, Germany

<sup>2</sup>Diamond Light Source Ltd, Harwell Science and Innovation Campus, Didcot OX11 0DE, Oxfordshire, UK

<sup>3</sup>Institute for Photon Science and Synchrotron Radiation, Karlsruhe Institute of Technology (KIT), 76344 Eggenstein-Leopoldshafen, Germany

**Abstract**—Among all iron oxides, hematite ( $\alpha\text{-Fe}_2\text{O}_3$ ), goethite ( $\alpha\text{-FeOOH}$ ), and ferrihydrite ( $\text{FeOOH}\cdot n\text{H}_2\text{O}$ ) are the most common mineral species. While immobilization of Mo<sup>6+</sup> by surface adsorption on ferric oxides has been studied extensively, the mechanisms of incorporation in their structure have been researched little. The objective of this study was to investigate the relation between Mo content and its structural incorporation in hematite, goethite, and six-line ferrihydrite by a combination of X-ray absorption spectroscopy (XAS), powder X-ray diffraction (pXRD), and inductively-coupled plasma optical emission spectrometry (ICP-OES). Synthesized in the presence of Mo, the hematite, goethite, and six-line ferrihydrite phases incorporated up to 8.52, 0.03, and 17.49 wt. % Mo, respectively. For hematite and goethite, pXRD analyses did not indicate the presence of separate Mo phases. Refined unit-cell parameters correlated with increasing Mo concentration in hematite and goethite. The unit-cell parameters indicated an increase in structural disorder within both phases and, therefore, supported the structural incorporation of Mo in hematite and goethite. Analysis of pXRD measurements of Mo-bearing six-line ferrihydrites revealed small amounts of coprecipitated akaganéite. X-ray absorption near edge structure (XANES) measurements at the Mo  $L_3$ -edge indicated a strong distortion of the MoO<sub>6</sub> octahedra in all three phases. Fitting of extended X-ray absorption fine structure (EXAFS) spectra of the Mo  $K$ -edge supported the presence of such distorted octahedra in a coordination environment similar to the Fe position in the investigated specimen. Incorporation of Mo<sup>6+</sup> at the Fe<sup>3+</sup>-position for both hematite and goethite resulted in the formation of one Fe vacancy in close proximity to the newly incorporated Mo<sup>6+</sup> and, therefore, charge balance within the hematite and goethite structures.

**Keywords**—EXAFS · Ferrihydrite · Goethite · Hematite · Iron oxides · Molybdenum · XANES · XAS

## INTRODUCTION

Molybdenum (Mo) occurs as a trace element in most soils but it is essential for nearly all known life forms on Earth (Neunhäuser et al. 2001; Mendel and Bittner 2006). Both in the global biogeochemical oxidation-reduction cycles of carbon, nitrogen, and sulfur (Stiefel 2002; Williams and Frausto da Silva 2002) and in the metabolism of living organisms (Bortels 1930) Mo holds a key position in the active sites of a wide range of metalloenzymes (Norrish 1975; Mendel and Bittner 2006).

The most abundant and only bioavailable Mo species in environmental systems is Mo<sup>6+</sup>, in the form of the molybdate anion ( $\text{MoO}_4^{2-}$ ) (Mendel and Bittner 2006). In contrast to the oceans, where Mo concentrations are up to 10.3 mg/kg (Wang et al. 2011), the soil contains only 1–5 mg of Mo kg<sup>-1</sup> (He et al. 2005). Most soil-bound Mo is considered to not be bioavailable (Žemberyová et al. 2010) because of surface adsorption (Goldberg et al. 1996) or structural incorporation (Richmond et al. 2004; Carroll and Richmond 2008; Das et al. 2016) in the soil minerals. Various studies have

emphasized the adsorption mechanisms of Mo to different soil constituents (e.g. Goldberg et al. 1996; Brinza et al. 2008), whereas information about the structural incorporation of Mo in minerals remains scarce (Richmond et al. 2004; Carroll and Richmond 2008; Žemberyová et al. 2010; Wang et al. 2011; Brinza et al. 2015; Das et al. 2016).

Fixation of Mo in German forest soils by ferric oxides was documented by Lang and Kaupenjohann (1999) who showed that most Mo in these soils is not adsorbed but rather is associated with crystalline iron oxides (135–1071  $\mu\text{g}/\text{kg}$ ). The easily exchangeable Mo fraction amounts to only 5–28  $\mu\text{g}/\text{kg}$  and the poorly crystalline iron oxides retain 44–407  $\mu\text{g}/\text{kg}$ . Furthermore, shortly after Mo fertilization, forest soils retain molybdenum by surface adsorption to iron oxides, while, with increasing time, Mo is incorporated into the iron oxide structure and thus becomes inaccessible for further biogeochemical processes (Lang 2000).

Common iron oxide mineral phases in soils are goethite ( $\alpha\text{-FeOOH}$ ), lepidocrocite ( $\gamma\text{-FeOOH}$ ), ferrihydrite ( $\delta\text{-FeOOH}$ ), hematite ( $\alpha\text{-Fe}_2\text{O}_3$ ), maghemite ( $\gamma\text{-Fe}_2\text{O}_3$ ), magnetite ( $\text{Fe}_3\text{O}_4$ ), and ferrihydrite ( $\text{FeOOH}\cdot n\text{H}_2\text{O}$ ). Not only do they have large adsorption capacities for trace elements in solution (Peacock and Sherman 2004; Rout et al. 2012) but also for element uptake via coprecipitation (Martínez and McBride 1998, 2001; Manceau et al. 2000). These properties make them well known scavengers

\* E-mail address of corresponding author: marcel.goern@uni-jena.de

DOI: 10.1007/s42860-021-00116-x

© The Author(s) 2021

for metals (Dardenne et al. 2002; Tarassov et al. 2002; Mullet et al. 2007) and metalloids (e.g. Sieber et al. 1985; Scheinost et al. 2006; Bolanz et al. 2013b) in both natural and contaminated environments (Hochella et al. 2005). Iron oxide phases can, therefore, control the bioavailability of nutrients as well as contaminants such as arsenic (Sherman and Randall 2003; Bolanz et al. 2013a, b) and lead (Vu et al. 2010) in soils.

Previous studies focused predominantly on homovalent and homotopic substitutions, where  $\text{Fe}^{3+}$  is replaced by other trivalent cations such as  $\text{Al}^{3+}$ ,  $\text{Cr}^{3+}$ , or  $\text{Mn}^{3+}$  (Cornell and Giovanoli 1987; Wells et al. 2001; Mullet et al. 2007). The substitution by aliovalent cations such as  $\text{Mo}^{6+}$ , however, depends on intrinsic charge-balancing reactions. Several mechanisms were described or assumed in previous investigations, such as the formation of  $\text{Fe}^{3+}$  vacancies (Ciobanu et al. 2013), reduction of surrounding  $\text{Fe}^{3+}$  to  $\text{Fe}^{2+}$  (Balko and Clarkson 2001), the formation of  $\text{O}^{2-}$  vacancies (Khan et al. 2008), and the formation of structural clusters intergrown within the iron oxide host phase (Bolanz et al. 2013b). For  $\text{Mo}^{6+}$ , the most abundant Mo species in oxic systems (Barron et al. 2009), almost no convincing data for structural incorporation in iron oxides exist, however.

The objective of the current study was to investigate the mechanisms of structural incorporation of Mo in ferrihydrite, goethite, and hematite. Synthesis protocols for these Mo-bearing iron oxides needed to be developed, therefore, and the resulting products needed to be analyzed by XAS. The research focused on: (1) developing reproducible methods to synthesize Mo-bearing iron oxides; (2) evaluating the mechanisms of structural incorporation of  $\text{Mo}^{6+}$  in these oxides; and (3) assessing the effects of  $\text{Mo}^{6+}$  incorporation on the structures of iron oxides.

## METHODS

### *Synthesis of Pure and Mo-bearing Iron Oxides*

The investigated iron oxides were synthesized in the absence or presence of  $\text{Mo}^{6+}$  according to modified procedures described by Schwertmann and Cornell (2000). All of the chemicals (which have the brand name Emsure®) were supplied by Merck (Germany) and met ACS, Reag. Ph. Eur., and ISO guidelines for analytical-grade chemicals.

For the synthesis of pure six-line ferrihydrite, 20 g of iron(III) nitrate nonahydrate was dissolved in 1.5 L deionized water preheated to 75°C, under rapid stirring. Immediately afterward, the solution was placed in an oven for 10 min at 75°C. During this time, the solution changed from amber-colored to dark reddish brown. The dark brown solution was plunged into ice water for rapid cooling. For Mo-bearing six-line ferrihydrite, selected volumes of a  $\text{Na}_2\text{MoO}_4 \cdot 2\text{H}_2\text{O}$  solution adjusted to pH 4 with diluted  $\text{HNO}_3$  were added to previously-made iron(III) nitrate nonahydrate solution. The Mo:Fe molar ratios used were 0 (blank), 0.01, 0.02, 0.05, and 0.10.

The formation of hematite was based on the transformation of two-line ferrihydrite and started with the synthesis of pure and Mo-bearing ferrihydrite. 20 g of iron(III) nitrate nonahydrate ( $\text{Fe}(\text{NO}_3)_3 \cdot 9\text{H}_2\text{O}$ ) was dissolved in 300 mL of deionized water under vigorous stirring. For Mo-bearing two-line ferrihydrite, selected volumes of a  $\text{Na}_2\text{MoO}_4 \cdot 2\text{H}_2\text{O}$  solution, previously adjusted to pH 4 with diluted  $\text{HNO}_3$ , were added, so that the following initial Mo:Fe molar ratios applied: 0 (blank), 0.01, 0.02, 0.05, 0.10, 0.20, 0.50, and 1.00. Subsequent addition of a 1 M KOH solution raised the pH to 7–8 and the solution changed from amber to a dark brown suspension of two-line ferrihydrite. These ferrihydrite suspensions were filtered and the still moist, thick filtrate was transferred into 100 mL pressure reaction vessels and placed in a preheated oven at 200°C for 7 days.

For the synthesis of goethite, a method based on the transformation of ferrihydrite was suggested by Schwertmann and Cornell (2000). There, 50 mL of a 1 M iron(III) nitrate nonahydrate solution was poured into a 1 L polyethylene flask and 90 mL of 5 M KOH solution was added quickly under constant stirring. Reddish brown ferrihydrite precipitated immediately and the suspension was diluted to 1 L with deionized water. Aging of this suspension in a closed flask at 70°C for 3 days led to the transformation of ferrihydrite to ochreous goethite. Molybdenum in various Mo:Fe molar ratios was introduced by adding 50 mL of a pH 4-adjusted  $\text{Na}_2\text{MoO}_4 \cdot 2\text{H}_2\text{O}$  solution to the 50 mL of previously made 1 M iron(III) nitrate nonahydrate solution. After addition of 90 mL of 5 M KOH solution, the resulting Mo-bearing ferrihydrite suspension was left to age in a preheated oven at 70°C for 3 days.

All resulting suspensions and solids were treated with 200 mL of a 0.2 M solution of  $\text{K}_2\text{HPO}_4$  and  $\text{KH}_2\text{PO}_4$  (according to Liang and Zhu 2016) in order to desorb molybdate ions attached to the outer surface of the iron oxide particles. Subsequently, the suspensions were washed by dialysis for about a week until the conductivity of the dialysis solution, deionized water, decreased to  $<10 \mu\text{S}/\text{cm}$ , then filtered and air-dried. After drying, the precipitates were ground for ~10 min with an agate mortar and pestle and sealed in glass vials. In the case of six-line ferrihydrite, before starting the desorption step, the resulting suspension was washed by dialysis, dried in an oven at 30°C, and the dry product then ground. The powder obtained was added to 200 mL of the 0.2 M  $\text{K}_2\text{HPO}_4$  and  $\text{KH}_2\text{PO}_4$  solution and subsequently treated like the above-mentioned suspensions. If not implemented in this order, six-line ferrihydrite in suspension would transform to two-line ferrihydrite during desorption.

### *Powder X-ray Diffraction Analysis (XRD)*

Powder XRD patterns of all synthesized phases and reference compounds were collected with a Bruker D8 AXS Advance diffractometer (Bruker, Karlsruhe, Germany) using  $\text{CuK}\alpha$  radiation ( $\lambda = 1.5406 \text{ \AA}$ ) and equipped with a LYNXEYE detector. Samples of the pure iron oxides and the Mo-bearing samples were

measured for full-profile refinement at 20°C from 5 to 120°2 $\theta$  with a dwell time of 1 s and a step width of 0.01°2 $\theta$ . The powder XRD patterns were processed using the software *JANA2006* (Petříček et al. 2014), and for the fitting, models of six-line ferrihydrite (Michel et al. 2007), hematite (Blake et al. 1966), goethite (Gualtieri and Venturelli 1999), and akaganéite (Post et al. 2003) were used. The statistical measures of deviation of the fit from the data obtained are given in Table 1, including the residuals for the weighted profile ( $R_{wp}$ ) and the goodness-of-fit (GOF).

#### Inductively-coupled Plasma Optical Emission Spectrometry (ICP-OES)

A simultaneous radial ICP-OES spectrometer 725ES (Agilent Technologies, Waldbronn, Germany) with a charge-coupled device (CCD) detector was used to determine the chemical composition of all samples (Fe, Mo). Before measurements, each sample was dried at 105°C for 24 h. Subsequently, ~100 mg of each sample was dissolved at room temperature in 5 mL of concentrated hydrochloric acid (HCl), adjusted to a defined volume of 10 mL with deionized water and stored in corrosion-resistant sample tubes.

#### X-ray Absorption Near-edge Structure (XANES) and Extended X-ray Absorption Fine-structure (EXAFS) Spectroscopy

X-ray absorption near-edge structure (XANES) and extended X-ray absorption fine-structure (EXAFS) spectra of the synthesized Mo-bearing iron oxides and reference materials (MoO<sub>2</sub>, MoO<sub>3</sub>, and Na<sub>2</sub>MoO<sub>4</sub>·2H<sub>2</sub>O) were collected at the Mo *L*<sub>3</sub>-edge (2520 eV) at the SUL-X beamline of the Karlsruhe Research Accelerator (KARA), Germany, and at the Mo *K*-edge (20,020 eV) at the B18 beamline of the Diamond Light Source (Didcot, UK). A silicon (111) crystal pair with a fixed beam exit as monochromator was used for XANES and EXAFS measurements at the SUL-X and B18 beamlines.

Using the software *XAFSmass* (Klementiev 2012), a defined mass of each sample was calculated for optimum absorption and subsequently mixed with cellulose powder, homogenized, and pressed into pellets. This resulted in a Mo concentration of 2.710 wt.% for the six-line ferrihydrite, 2.733 wt.% for the hematite, and 0.013 wt.% for the goethite pellet.

The XANES spectra at the Mo *L*<sub>3</sub>-edge were collected at the SUL-X beamline with a step width of 5 eV in the region of -80 to -50 eV, 1 eV in the region -50 to -20 eV below

**Table 1** Chemistry, Fe loss per mole of Mo, and unit-cell parameters of pure and Mo-bearing phases as determined by ICP-OES and full profile fitting with the goethite structure by Gualtieri and Venturelli (1999) and the hematite structure by Blake et al. (1966)

Sample	Fe (wt.%)	Mo (wt.%)	Fe loss	<i>a</i> (Å)	<i>b</i> (Å)	<i>c</i> (Å)	Cell volume	$R_{wp}$	GOF
hem_0	67.75 ± 0.49	n.v.		5.03890(6)		13.7615(3)	302.60(1)	5.39	1.27
hem_0.01	67.25 ± 0.45	1.1199 ± 0.0052	0.76 ± 0.80*	5.03695(6)		13.7751(3)	302.663(3)	5.12	1.21
hem_0.02	66.51 ± 0.47	2.1564 ± 0.0249	0.98 ± 0.45*	5.03599(5)		13.7817(2)	302.693(8)	5.14	1.18
hem_0.05	64.54 ± 0.52	3.9047 ± 0.0289	1.41 ± 0.28*	5.03426(5)		13.7960(2)	302.800(8)	5.29	1.24
hem_0.1	62.72 ± 0.46	5.4993 ± 0.0548	1.57 ± 0.18*	5.03363(4)		13.7989(2)	302.787(6)	4.99	1.20
hem_0.2	59.90 ± 0.39	7.7111 ± 0.0695	1.75 ± 0.12*	5.03043(5)		13.8202(2)	302.870(8)	4.82	1.24
hem_0.5	60.20 ± 0.38	7.1541 ± 0.0497	1.81 ± 0.12*	5.03166(4)		13.8115(2)	302.828(6)	4.72	1.19
hem_1.0	57.34 ± 0.44	8.5240 ± 0.0894	2.10 ± 0.13*	5.03065(4)		13.8177(2)	302.840(6)	4.97	1.31
goe_0	62.11 ± 0.56	n.v.		9.9551(4)	3.0229(1)	4.6116(1)	138.781(9)	4.97	1.46
goe_0.05	61.56 ± 0.26	n.v.		9.9592(4)	3.0221(1)	4.6079(1)	138.69(1)	4.78	1.38
goe_0.1	61.29 ± 0.17	n.v.		9.9594(4)	3.0222(1)	4.6068(1)	138.661(9)	4.57	1.34
goe_0.25	61.77 ± 0.35	0.0150 ± 0.0015		9.9600(4)	3.0225(1)	4.6072(1)	138.695(8)	4.63	1.34
goe_0.5	61.02 ± 0.34	0.0212 ± 0.0004		9.9615(4)	3.0222(1)	4.6070(1)	138.697(8)	4.59	1.35
goe_0.75	61.64 ± 0.32	0.0259 ± 0.0001		9.9621(5)	3.0221(1)	4.6070(1)	138.70(1)	4.67	1.37
goe_1.0	61.34 ± 0.44	0.0274 ± 0.0005		9.9622(3)	3.0226(1)	4.6076(1)	138.744(6)	4.51	1.35
6L-Feh_0	57.33 ± 0.34	n.v.							
6L-Feh_0.01	45.14 ± 0.34	2.6072 ± 0.0074							
6L-Feh_0.02	44.25 ± 0.28	3.7133 ± 0.0398							
6L-Feh_0.05	37.07 ± 0.25	9.5864 ± 0.0997							
6L-Feh_0.1	31.97 ± 0.19	17.4853 ± 0.1546							

Values below the detection limit are marked n.v. (no value). Values marked with \* represent the estimated uncertainty for the Fe loss per mole of Mo. The numbers in parentheses indicate the uncertainty for the last digit. For each fit, the weighted R-factor ( $R_{wp}$ ) and goodness of fit (GOF) are given

the edge, 0.2 eV in the region  $-20$  to  $+20$  eV relative to the edge, and  $0.05 \text{ \AA}^{-1}$  up to  $5.3 \text{ k}$  ( $\sim 105 \text{ eV}$ ) above the absorption edge. EXAFS spectra collected at the Diamond Light Source were recorded with a step width of  $0.3 \text{ eV}$  in the region  $-200$  to  $1000 \text{ eV}$  relative to the edge ( $20,020 \text{ eV}$ ).

At KARA, all spectra were measured simultaneously in transmission and fluorescence mode, while spectra collected at Diamond were measured in transmission mode. A  $\text{Mo}^0$  foil was mounted between ionization chambers 2 and 3 at the beamlines. The Mo  $K$ - or  $L_3$ -edge was recorded parallel to each sample spectrum for energy calibration. Five spectra were measured for each sample as a minimum and two spectra for each reference compound.

All EXAFS spectra were processed and fit by the *Demeter* software package (Ravel and Newville 2005). For the shell-by-shell fitting of the  $k^3$ -weighted EXAFS spectra, paths generated from models of six-line ferrihydrite (Michel et al. 2007), a hematite supercell based on the structure of Blake et al. (1966), and a goethite supercell based on the structure of Gualtieri and Venturelli (1999) were used. In these models, Mo replaced one Fe atom. Parameters for the paths were calculated by FEFF6 (de Leon et al. 1991) from the *Demeter* software package (Ravel and Newville 2005).

The statistical measures of the deviation of the fit from data obtained are given, as well as the number of variables allowed (to float) in the fit ( $N_{\text{var}}$ ), the number of independent data points ( $N_{\text{idp}}$ ), and the R factor. While  $N_{\text{idp}}$  is equal to  $2\Delta kR/\pi$ , where  $k$  and  $R$  are the fitting ranges, the R factor is defined as:

$$R = \frac{\sum [\chi_i^{\text{data}} - \chi_i^{\text{model}(x)}]^2}{\sum [\chi_i^{\text{data}}]^2} \quad (1)$$

where  $\chi$  is the magnitude of the EXAFS oscillations and  $x$  is the set of variables to be refined.

The EXAFS spectra of the references were fitted with the respective structures. Their spectra were used to identify problems that could be encountered when fitting a model to the structurally unknown samples.

## RESULTS

### Chemical Composition of Pure and Mo-bearing Iron Oxides

The chemical compositions of all synthesized iron oxide phases, obtained by ICP-OES, showed an increase in the Mo content in the solid phase with the increasing initial Mo:Fe molar ratio in solution (Table 1).

Goethite takes up less Mo than any of the other phases studied. Synthesized at an initial Mo:Fe molar ratio of 1.0, goethite contained only 0.03 wt.% Mo. In comparison, six-line ferrihydrite or hematite synthesized at an initial Mo:Fe ratio of 0.01 contained much more Mo, 2.61 or 1.12 wt.%, respectively. Despite their low Mo concentrations, the goethite samples were included in this study because crystallographic changes in the samples could still be observed. For hematite with larger Mo concentrations, the molar loss of Fe for each mole of Mo ( $Fe_{\text{loss}}$ ) was calculated by (Bolanz et al. 2017):

$$Fe_{\text{loss}} = \frac{(Fe_{\text{wt.\%}}^{\text{Mo}(0)} - Fe_{\text{wt.\%}}^{\text{Mo}(x)}) \times M_{\text{Mo}}}{Mo_{\text{wt.\%}}^{\text{Mo}(x)} \times M_{\text{Fe}}} \quad (2)$$

where  $Fe_{\text{wt.\%}}^{\text{Mo}(0)}$  is the Fe content of the Mo-free six-line ferrihydrite or hematite in wt.% and  $Fe_{\text{wt.\%}}^{\text{Mo}(x)}$  stands for

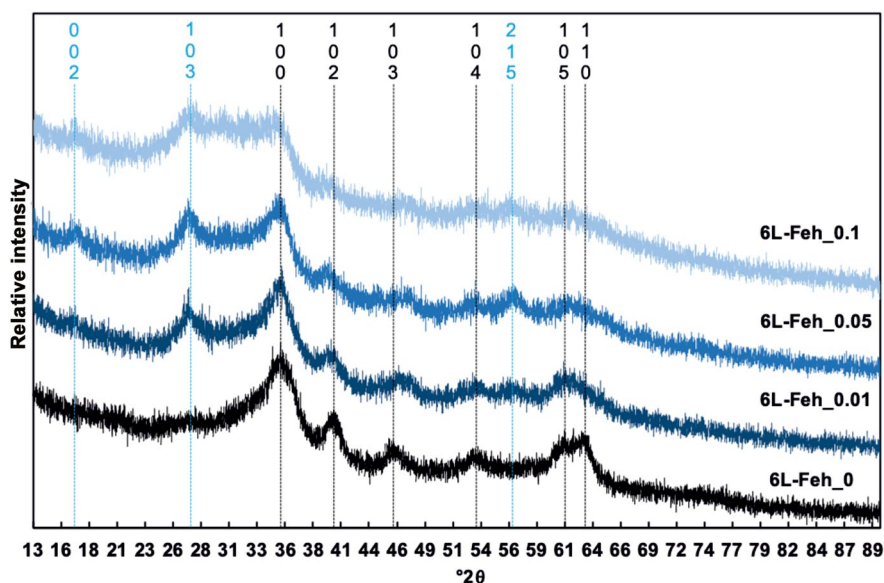


**Fig. 1** Powder XRD patterns of six-line ferrihydrite synthesized in the absence of  $\text{Mo}^{6+}$  and selected samples grown at initial Mo:Fe molar ratios of 0.01, 0.05, and 0.1 display the increase of akaganéite with increasing Mo:Fe ratios. Miller indices for six-line ferrihydrite (black) were taken from Jansen et al. (2002), and for akaganéite (blue) from Post et al. (2003)

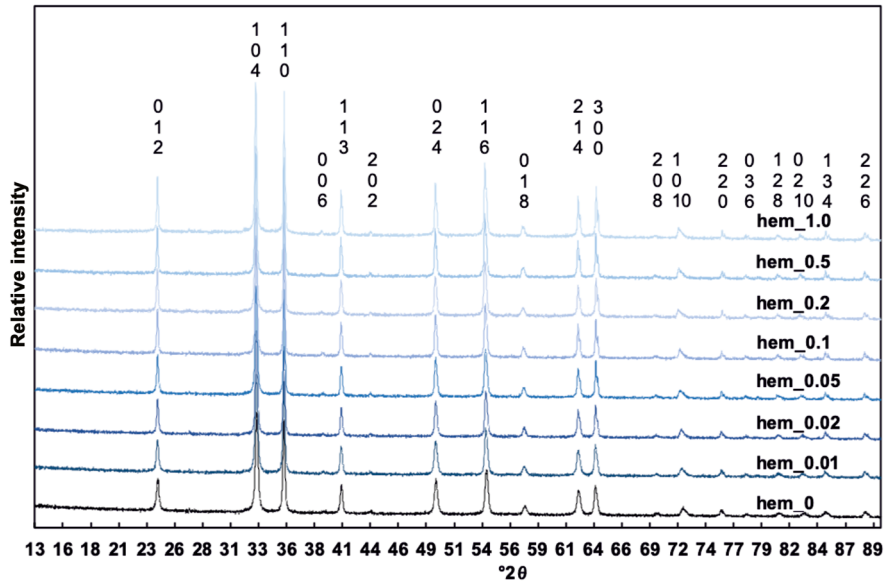


Fig. 2 Powder XRD patterns of hematite synthesized in the absence of Mo<sup>6+</sup> and samples grown at initial Mo:Fe molar ratios of 0.01, 0.02, 0.05, 0.1, 0.2, 0.5, and 1.0. Miller indices were taken from Blake et al. (1966)

the Fe content of Mo-bearing six-line ferrihydrite or hematite,  $M_{Mo}$  and  $M_{Fe}$  are the molecular weights of Mo and Fe, respectively, and  $Mo_{wt\%}^{Mo(x)}$  is the Mo content in wt.% of the Mo-bearing hematite.

The results of the calculations for the synthesized hematite showed that the Fe loss per mole of Mo incorporated (Table 1) increased from ~0.76 at low initial Mo:Fe molar

ratios in hem\_0.01 to ~2.10 in hem\_1.0, where the initial Mo:Fe molar ratio used for synthesizing this sample was 1.0.

Because no Mo-bearing six-line ferrihydrite could be synthesized as a pure single phase and in spite of their large Mo concentrations, no calculations were done for the loss of Fe per Mo atom incorporated.

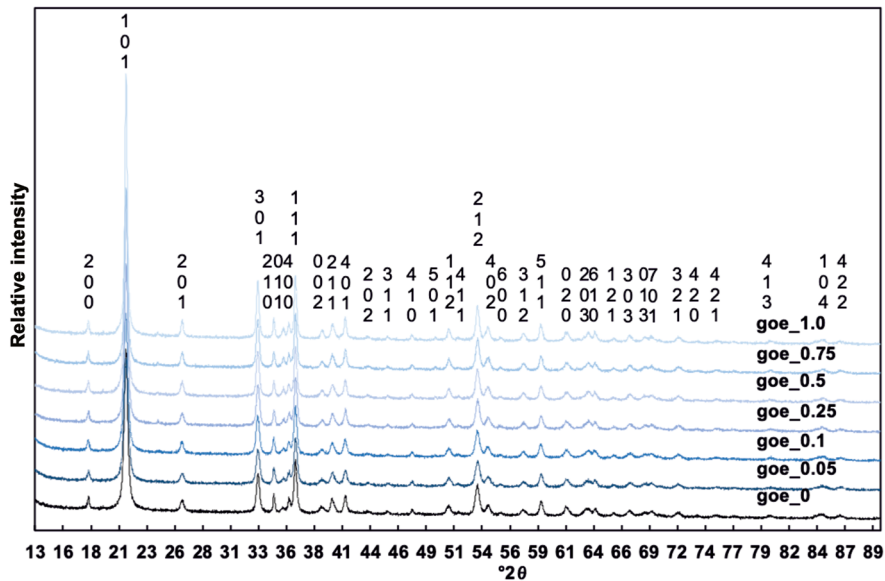


Fig. 3 Powder XRD patterns of goethite synthesized in the absence of Mo<sup>6+</sup> and samples grown at initial Mo:Fe molar ratios of 0.05, 0.1, 0.25, 0.5, 0.75, and 1.0. Miller indices were taken from Gualtieri and Venturelli (1999)

### Powder X-ray Diffraction

Powder XRD patterns of six-line ferrihydrites at various initial Mo:Fe molar ratios (0, 0.01, 0.05, 0.1) (Fig. 1) revealed that akaganéite ( $\beta$ -FeOOH) was present as an impurity in the samples, documented by pXRD peaks at  $\sim 17$  (Bragg indices 002),  $\sim 27$  (103), and  $\sim 57$  (215) $^\circ 2\theta$ . The intensities of the akaganéite peaks increased with increasing initial Mo:Fe molar ratios. Low intensities and very broad peaks testified to the poor crystallinity of both products and prevented quantitative evaluation of lattice parameters or phase fractions. Only syntheses up to an initial Mo:Fe molar ratio of 0.1 were considered further. The pXRD data showed that higher Mo:Fe ratios resulted in the precipitation of two-line ferrihydrite instead of six-line ferrihydrite.

Powder XRD patterns of the synthesized hematite (Fig. 2) and goethite (Fig. 3) samples displayed only XRD maxima characteristic of each individual phase. The refined lattice parameters and cell volumes of the full-profile fits are given in Table 1. For hematite, in particular, the unit-cell dimensions correlated strongly with the Mo content. The lattice parameter  $c$  and the cell volume increased from 13.7615(3) Å and 302.60 Å<sup>3</sup> in the absence of Mo to 13.8177(2) Å and 302.84 Å<sup>3</sup> at an initial Mo:Fe molar ratio of 1.0. On the contrary, the lattice parameter  $a$  decreased from 5.03890(6) Å for pure hematite to 5.03065(4) Å for hem\_1.0 (Table 1, Fig. 4a). Expansion of the lattice parameter  $c$  agreed with observations for hematite grown in the presence of P<sup>5+</sup> (Gálvez et al. 1999) and As<sup>5+</sup> (Bolanz et al. 2013b).

For goethite, the lattice parameter  $a$  increased from 9.951(4) Å in the absence of Mo to 9.9622(3) Å at an initial Mo:Fe molar ratio of 1; parameter  $c$  showed negative correlation with increasing Mo content (Fig. 4b). Unit-cell parameter  $b$  and the cell volume did not correlate with the Mo concentration.

### X-ray Absorption Near-edge Structure (XANES) Spectroscopy

Normalized Mo  $K$ -edge XANES profiles of the synthesized phases (Fig. 5) showed almost the same pattern with a distinct pre-edge feature at  $\sim 19,996.0$  eV, the absorption edge at  $\sim 20,006.4$  eV, and the crest of the white line at  $\sim 20,028.4$  eV. Based on the intensity of their pre-edge feature, the samples were divided into two groups. The first group comprised only the spectrum of sample goe\_1.0. This spectrum showed a more distinct pre-edge feature than the spectra of hematite and six-line ferrihydrite (Fig. 5) and a slightly less pronounced feature directly before the crest of the white line. In these features, it resembled the spectrum of Na<sub>2</sub>MoO<sub>4</sub>·2H<sub>2</sub>O where hexavalent Mo is in tetrahedral coordination with oxygen. The second group includes the spectra of hematite and six-line ferrihydrite. Their pre-edge features resembled more those in MoO<sub>3</sub>, which consists of layers of MoO<sub>6</sub> octahedra in an orthorhombic crystal. None of the samples investigated resembled MoO<sub>2</sub> which crystallizes in a monoclinic cell and has a rutile-like structure consisting of distorted Mo(IV) octahedra.

The XANES spectra at the Mo  $L_3$ -edge showed splitting of the white line which is a function of Mo coordination (Fig. 6). The first peak was always more intense than the second one, but the energy differences between the peaks (i.e. peak-splitting values) differed considerably. Hematite spectra showed the greatest values with 3.21–3.27 eV, followed by six-line ferrihydrite with 2.96–3.01 eV. The values for the goethite spectra were considerably smaller than for the other two samples with 2.60–2.82 eV, respectively.

### Extended X-ray Absorption Fine Structure (EXAFS) Spectroscopy at the Mo $K$ -edge

*Local Mo structure in six-line ferrihydrite.* As seen in the pXRD analyses (Fig. 1), six-line ferrihydrite was contaminated by a small amount of akaganéite. All X-ray absorption spectra of these samples were affected by this two-component system. Detailed evaluation of the local structure of Mo in six-line ferrihydrite was complicated. Fitting of the recorded EXAFS spectra sufficed for a general statement concerning the coordination of Mo in this structure and its surrounding short-range order.

Comparison of the EXAFS spectra of pure Mo-bearing akaganéite with the six-line ferrihydrite/akaganéite mixture (Fig. 7) showed that the first shell of both spectra matched well, while the second-shell features of both samples located between 2.2 and 3.4 Å (uncorrected for phase

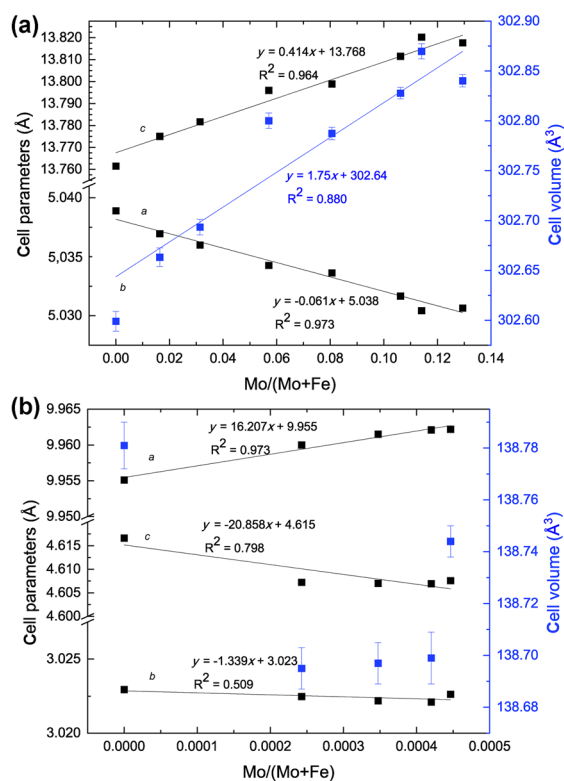


**Fig. 4** Comparison of unit-cell parameters of **a** hematite and **b** goethite. Error bars of cell parameters are smaller than the symbols

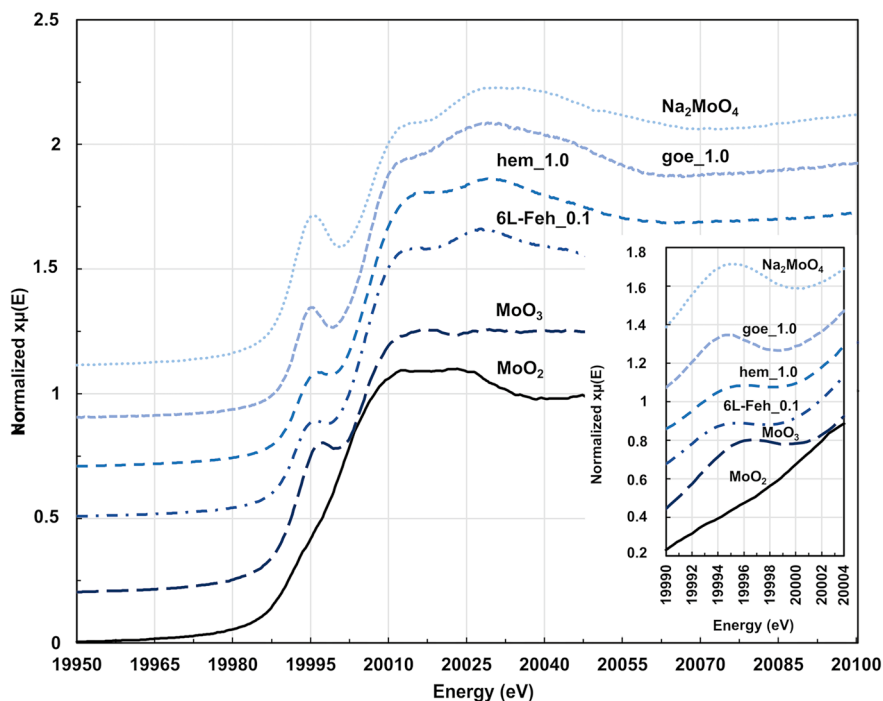


**Fig. 5** Normalized Mo *K*-edge XANES spectra of the synthesized phases goe\_1.0, hem\_1.0, and 6L-Feh\_0.1 and reference substances MoO<sub>2</sub>, MoO<sub>3</sub>, and Na<sub>2</sub>MoO<sub>4</sub>. A more detailed section showing the pre-edge feature of the spectra is inset. Each spectrum represents the average of at least three spectra

shift) were significantly different. This difference enabled analysis of the position of Mo in the structure of six-line ferrihydrite.

Although the XANES measurements suggested octahedral Mo coordination, fitting of Mo in both octahedral and tetrahedral coordination with the structural model of ferrihydrite from Michel et al. (2007) was implemented. In this model, Fe exists in two different octahedrally coordinated sites (Fe(1) and Fe(2)) and one tetrahedral site Fe(3).

The fitting results for octahedral Mo<sup>6+</sup> at the Fe(1) site suggested Mo–O distances of between 1.788(2) and 2.293(3) Å (corrected for phase shift, Table 2), which are consistent with the strongly distorted MoO<sub>6</sub> octahedron in sardignaita (Orlandi et al. 2010) used by Bolanz et al. (2017) to fit the first shell of Mo-substituted akaganéite. While the next Fe neighbors coordinated with Mo within the akaganéite structure of Bolanz et al. (2017) are at 3.311, 3.510, and 3.640 Å (two atoms for each path), the fitting results of the ferrihydrite model showed two additional groups of two Fe atoms at 2.860(2) Å and 3.068(2) Å. To compensate for the strongly distorted MoO<sub>6</sub> octahedron, the six remaining Fe atoms split into four Mo–Fe paths with different interatomic distances ranging from 3.204(5) to 3.663(7) Å. All paths of the Fe shell shared one value for the Debye–Waller factor ( $\sigma^2$ ), but had different  $\Delta r$  values except two groups of Fe atoms at distances of 2.860(2), 3.068(2), and 3.224(2) Å, as well as 3.569(7) and 3.663(7)

Å, respectively. The formation of Fe vacancies as described for akaganéite by Bolanz et al. (2017) was not observed.

With Mo–O distances of between 1.764(2) and 2.362(8) Å (corrected for phase shift, Table 3), the fitting results for octahedral Mo<sup>6+</sup> at the Fe(2) site were in good agreement with the observed values at the Fe(1) site. In contrast to the fit at the Fe(1) site, no Fe atoms were observed between 2.8 and 3.2 Å. The first two Fe atoms of the second shell were located at 3.209(1) Å. The incorporation of the strongly distorted MoO<sub>6</sub> octahedron at the Fe(2) site resulted in a considerable shift of the last seven Mo–Fe paths. These paths were longer than the corresponding calculated Fe–Fe distances. The three furthestmost Mo–Fe paths, which were split, showed distances of 3.667(9) and 3.823(1) Å, respectively. The calculated Fe–Fe distances, however, were located at 3.598 Å. All paths of the Fe shell shared the same Debye–Waller factor, which was smaller than that for Mo<sup>6+</sup> fit at the Fe(1) site. This could imply that the incorporation of Mo<sup>6+</sup> at the Fe(2) site leads to lower structural disorder than for Fe(1).

When considering suitable sites for the incorporation of Mo<sup>6+</sup> into the structure of six-line ferrihydrite, the coordination number of Mo<sup>6+</sup> is essential, either tetrahedral or octahedral (Shannon 1979). Short distances of ~1.7–1.8 Å were considered to be typical for tetrahedral coordination and longer distances of 1.9–2.1 Å indicated octahedral coordination.

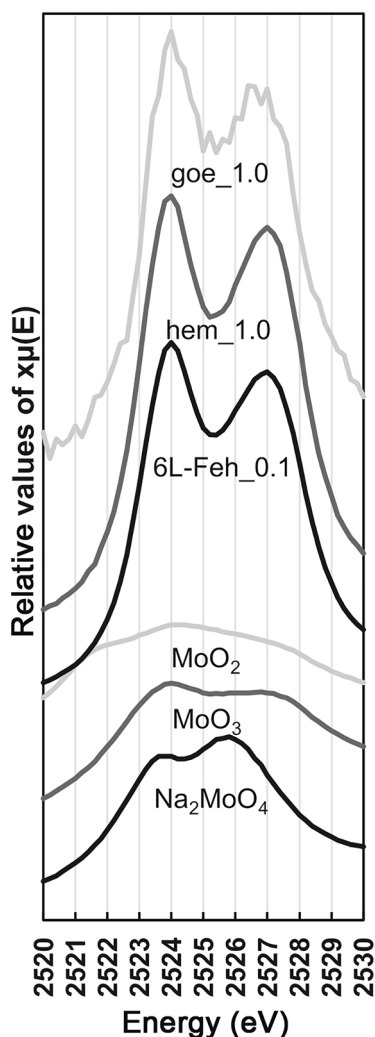


**Fig. 6** Normalized XANES spectra at the  $L_3$ -edge of samples goe\_1.0, hem\_1.0, and 6L-Feh\_0.1 and reference substances  $\text{MoO}_2$ ,  $\text{MoO}_3$ , and  $\text{Na}_2\text{MoO}_4$ . While  $\text{MoO}_2$  shows no distinctive peak-splitting, the splitting and the ratios between the intensities of both peaks for  $\text{MoO}_3$  (3:2) and  $\text{Na}_2\text{MoO}_4$  (2:3) are characteristic of Mo in octahedral and tetrahedral coordination, respectively

For six-line ferrihydrite, fitting with tetrahedral Mo (Fig. 8) resulted in significant distortion of the  $\text{MoO}_4$  tetrahedron. The distances of three Mo–O paths (1.783(2) Å) were shorter than calculated Fe–O distances (1.953 Å) for a Mo-free model; the fourth O atom at 2.052(9) Å was far more distant than O atoms typical for tetrahedral  $\text{Mo}^{6+}$  coordination. The Mo–Fe distances with bridging O atoms with short Mo–O distances were also relatively short, and *vice versa* (Table 4).

In summary, a model with tetrahedral  $\text{Mo}^{6+}$  in six-line ferrihydrite led to an exceptional distortion of the

tetrahedron and its surroundings. The goodness of fit ( $R_{\text{Fe}(3)}=0.027$ ) was worse than the fit with octahedral  $\text{Mo}^{6+}$  ( $R_{\text{Fe}(1)}=0.007$  and  $R_{\text{Fe}(2)}=0.003$ ). Hence, fitting with octahedral  $\text{Mo}^{6+}$  yielded significantly better results.

**Local Mo structure in hematite.** The Mo XANES spectra suggested octahedral  $\text{Mo}^{6+}$  coordination in the synthetic hematite. The EXAFS spectrum of the sample hem\_1.0 was fitted with paths calculated from a hematite supercell (based on the structure of Blake et al. 1966), in which one Mo replaces one Fe (Fig. 9). Due to the significant distortion of the  $\text{MoO}_6$  octahedron, the six O atoms of the first shell were fitted with three different Mo–O paths and distances of 1.790(3), 2.067(6), and 2.312(2) Å. All three paths were assigned the same amplitude and Debye-Waller factor, but different individual values for  $\Delta r$ . The path calculated for the face-sharing  $\text{Fe}^{3+}$  was excluded because such a close position of highly charged cations ( $\text{Mo}^{6+}$ – $\text{Mo}^{6+}$  or  $\text{Fe}^{3+}$ – $\text{Mo}^{6+}$ ) is unlikely. The second shell consisted of Fe atoms forming edge-sharing octahedra with distances of 3.169(8) Å and corner-sharing octahedra at 3.412(9) Å. They shared the same  $\sigma^2$ , but had different values for  $\Delta r$ . This approach improved the fit significantly and created an Fe vacancy for charge balance. The deviation of the interatomic distances in the third Fe shell with 5.30(2) Å, compared to 5.44 Å for Mo-free hematite, were significant despite the overall distance. These differences may indicate different degrees of Mo substitution in the hematite structure (Brinza et al. 2015).

**Local Mo structure in goethite.** For goethite,  $\text{Mo}^{6+}$  was modeled in both tetrahedral and octahedral coordination (Fig. 9). For Mo in tetrahedral coordination, the EXAFS spectrum of sample goe\_1.0 was fitted with the calculated paths of a combined model of a goethite (Gualtieri and Venturelli 1999) supercell and the structure of  $\text{FeMoO}_4$  (Rapposch et al. 1980). The fitting shows that  $\text{Mo}^{6+}$  was surrounded by four oxygen atoms at a distance of 1.780(2) Å (Table 5), at the higher end of the range of Mo–O distances in  $\text{FeMoO}_4$  (1.633–1.779 Å). Fitting of the second shell was performed using the structure of a goethite supercell. The addition of the eight nearest Fe atoms (at Mo–Fe distances of 3.023 to 3.584 Å) and all attempts to refine this model worsened the goodness of fit significantly. Other alternatives were sought, therefore, to explain the second shell features at 2.2–2.5 and 2.7–3.4 Å (uncorrected for phase shift) of the EXAFS spectrum (Fig. 9). The notion of tetrahedral incorporation of  $\text{Mo}^{6+}$  in the goethite structure was abandoned and replaced by a model (Table 5) in which tetrahedral  $\text{MoO}_4^{2-}$  was adsorbed onto goethite. Fitting of  $\text{Mo}^{6+}$  as tetrahedrally adsorbed  $\text{MoO}_4^{2-}$  onto goethite resulted in Mo–Fe distances of 2.90(4) and 3.58(2) Å, both with different values for  $\sigma^2$  (Table 5). The goodness of fit was  $R=0.079$ .

For comparison,  $\text{Mo}^{6+}$  was also modeled in octahedral coordination (Fig. 9). Paths created by a



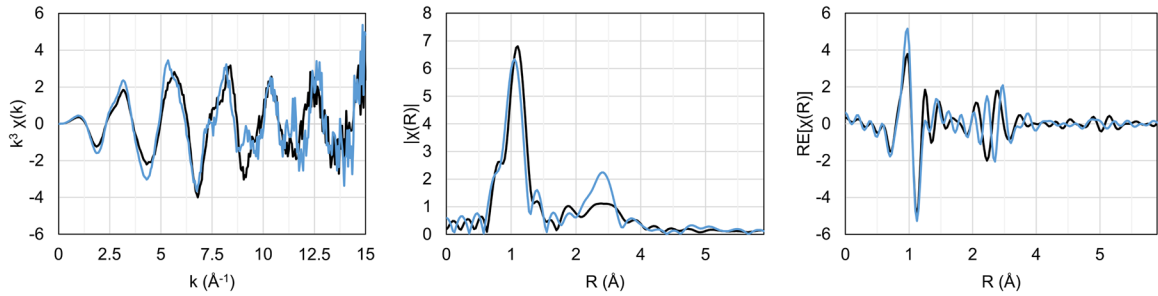


**Fig. 7** Normalized  $k^3$ -weighted Mo  $K$ -edge spectra (left), magnitude of the Fourier transform (middle), and part of the Fourier transform of the Mo  $K$ -edge spectra (right). The thick black lines represent the measured and processed data of 6L-Feh\_0.1, the blue lines represent the akaganéite data. All spectra are uncorrected for phase shift

Mo-bearing goethite supercell to fit this model resulted in five different Mo–O paths (Table 6) for octahedrally coordinated  $\text{Mo}^{6+}$ . The Mo–O distances in the first shell ranged from 1.783(5) Å to 2.29(2) Å. The second shell consisted of four edge- and four corner-sharing Fe octahedra with Mo–Fe distances of 2.93(2) and 3.32(3) Å, both for the edge-sharing octahedra, and 3.59(1) Å for the corner-sharing ones, respectively. Removing one of the closest Fe atoms from the fit (located at 2.93(2) Å) reduced the amplitude of the second shell feature at 2.2–2.5 Å and, therefore, improved the fit significantly. The goodness of this fit was with  $R=0.036$ , less than half that of the fit for tetrahedral  $\text{MoO}_4^{2-}$  adsorbed to goethite ( $R=0.079$ ) and, therefore, in better agreement with the measured EXAFS spectrum of goe\_1.0.

**Table 2** Scattering paths for octahedrally coordinated  $\text{Mo}^{6+}$  in six-line ferrihydrite (6L-Feh\_0.1) at the Fe(1) site

Single scattering paths	$N$	$d$ (Å)	$\sigma^2$
Mo–O	1	1.788 ± 0.002	0.006
Mo–O	2	1.788 ± 0.004	0.006
Mo–O	1	2.031 ± 0.005	0.006
Mo–O	1	2.114 ± 0.006	0.006
Mo–O	1	2.293 ± 0.003	0.006
Mo–Fe	2	2.860 ± 0.002	0.013
Mo–Fe	2	3.068 ± 0.002	0.013
Mo–Fe	2	3.204 ± 0.005	0.013
Mo–Fe	1	3.324 ± 0.002	0.013
Mo–Fe	1	3.569 ± 0.007	0.013
Mo–Fe	2	3.663 ± 0.007	0.013
Mo–O	2	3.847 ± 0.005	0.001

$\Delta E_0=0$ ,  $N_{\text{var}}=14$ ,  $N_{\text{ind}}=28$ ,  $R=0.007$ ,  $k$ -range=3–12,  $R$ -range=1.000–6.000

## DISCUSSION

### Six-line Ferrihydrite

Powder XRD measurements of the synthesized Mo-bearing six-line ferrihydrites indicated the coprecipitation of chlorine-free akaganéite, as described previously by Linehan et al. (1997), Richmond et al. (2004), and Carroll and Richmond (2008). All further compositional and structural investigations were, therefore, affected by this two-component system.

Comparing the Mo  $L_3$ -edge XANES spectra of the six-line ferrihydrite phases with spectra of Mo-bearing akaganéite of Bolanz et al. (2017) showed that the peak-splitting values of the synthesized samples (2.96 to 3.01 eV) were considerably greater than the 2.7 eV measured for akaganéite (Bolanz et al. 2017).  $\text{Mo}^{6+}$  was, therefore, considered to be octahedrally coordinated in six-line ferrihydrite. Nevertheless,

**Table 3** Scattering paths for octahedrally coordinated  $\text{Mo}^{6+}$  in six-line ferrihydrite (6L-Feh\_0.1) at the Fe(2) site

Single scattering paths	$N$	$d$ (Å)	$\sigma^2$
Mo–O	2	1.764 ± 0.002	0.002
Mo–O	1	1.919 ± 0.010	0.002
Mo–O	1	2.088 ± 0.009	0.002
Mo–O	1	2.199 ± 0.009	0.002
Mo–O	1	2.362 ± 0.008	0.002
Mo–Fe	2	3.209 ± 0.001	0.007
Mo–Fe	1	3.346 ± 0.003	0.007
Mo–Fe	3	3.430 ± 0.001	0.007
Mo–Fe	4	3.601 ± 0.005	0.007
Mo–Fe	1	3.667 ± 0.009	0.007
Mo–Fe	2	3.823 ± 0.001	0.007

$\Delta E_0=0$ ,  $N_{\text{var}}=14$ ,  $N_{\text{ind}}=28$ ,  $R=0.003$ ,  $k$ -range=3–12,  $R$ -range=1.000–6.000

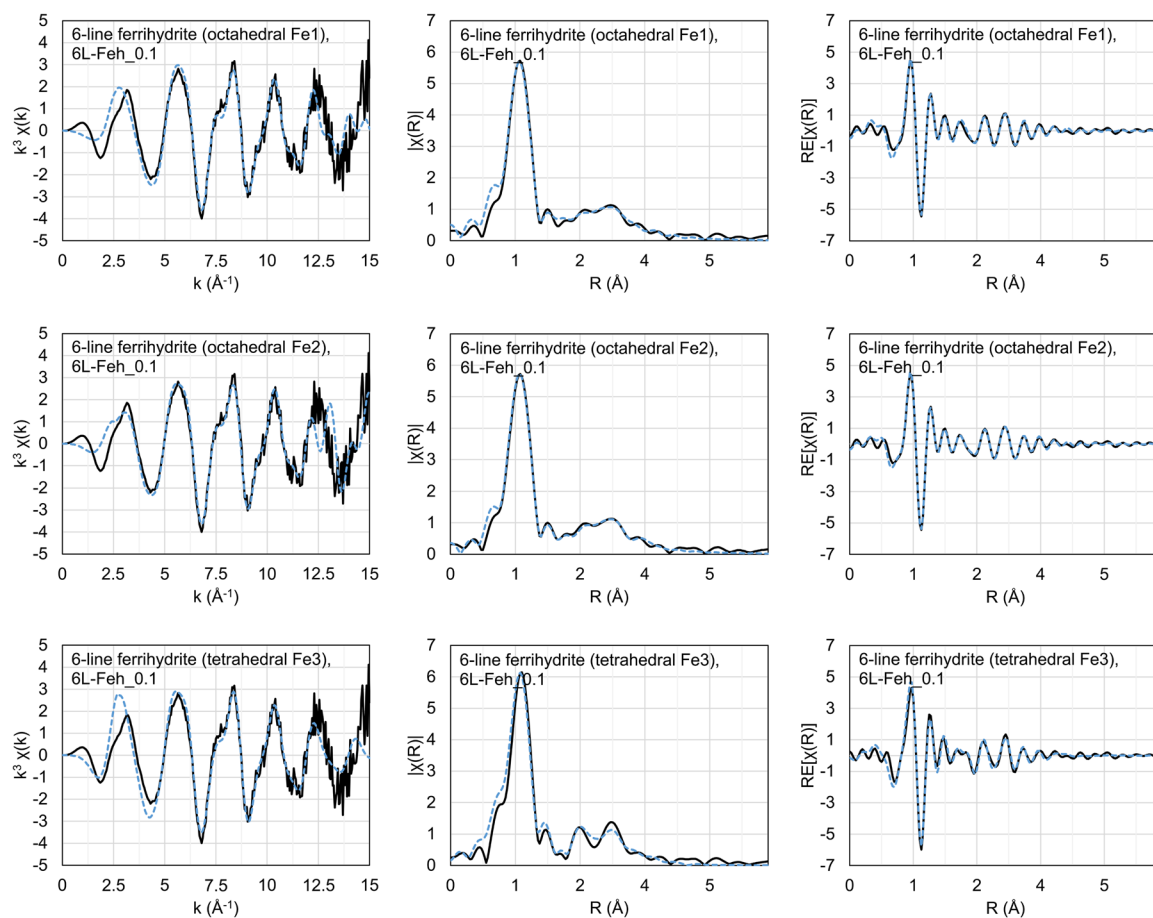


**Fig. 8** Normalized  $k^3$ -weighted Mo  $K$ -edge spectra (left), magnitude of the Fourier transform (middle), and part of the Fourier transform of the Mo  $K$ -edge spectra (right). The thick black lines represent the measured and processed data of 6L-Feh\_0.1, the dashed blue lines represent the fits. All spectra are uncorrected for phase shift

because of the generally low peak-splitting values, the possibility of tetrahedrally incorporated  $\text{Mo}^{6+}$  was still checked.

Fitting of the EXAFS spectra with Mo in octahedral and tetrahedral coordination suggested that octahedral  $\text{Mo}^{6+}$  led to a better fit, applying the structure of Michel et al. (2007). The formation of  $\text{Fe}^{3+}$  vacancies as described by Bolanz et al. (2017) for akaganéite or as for hematite (this study) was not observed. Possible ways to balance the excess charge of  $\text{Mo}^{6+}$  could be the release of three  $\text{H}^+$  atoms or the incorporation of three additional hydroxide ions ( $\text{OH}^-$ ) in the structure of ferrihydrite, which still is not fully understood. Compared to listed values of Mo–O distances for  $\text{MoO}_4$  tetrahedra in other phases (Table 7), the incorporation of tetrahedrally coordinated  $\text{Mo}^{6+}$  in six-line ferrihydrite resulted in significant distortion of the  $\text{MoO}_4$  tetrahedron. The longest Mo–O distance, 1.87(2) Å for  $(\text{NH}_4)_8\text{Mo}_{10}\text{O}_{34}$  (Benchrifá and de Pape 1990), was still much shorter than 2.050(9) Å, the greatest distance

for the  $\text{MoO}_4$  tetrahedron modeled for six-line ferrihydrite. Distances of 1.9–2.1 Å are characteristic of octahedral coordination of Mo (Shannon 1979) and the incorporation of Mo in tetrahedral coordination would, therefore, result in the destabilization of said tetrahedron and its surroundings.

The authors admit, at this point, that neither the structure of Mo-bearing six-line ferrihydrite as a whole nor the corresponding charge-balance reaction could be resolved. Further experiments and a working method to synthesize pure Mo-bearing six-line ferrihydrite are needed, therefore.

#### Hematite

Refining of the hematite pXRD spectra resulted in notable changes in the unit-cell parameters  $a$  and  $c$  together with the increase in unit-cell volume with increasing the initial Mo:Fe molar ratio (Table 1). Similar changes were observed in studies

**Table 4** Scattering paths for tetrahedrally coordinated Mo<sup>6+</sup> in six-line ferrihydrite (6L-Feh\_0.1) at the Fe(3) site

Single scattering paths	<i>N</i>	<i>d</i> (Å)	σ <sup>2</sup>
Mo–O	3	1.783 ± 0.002	0.006
Mo–O	1	2.052 ± 0.009	0.006
Mo–O	3	2.832 ± 0.015	0.013
Mo–Fe	3	3.163 ± 0.005	0.011
Mo–Fe	3	3.306 ± 0.005	0.011
Mo–Fe	3	3.404 ± 0.006	0.011
Mo–Fe	1	3.566 ± 0.023	0.011
Mo–Fe	3	3.569 ± 0.007	0.011
Mo–O	3	3.550 ± 0.029	0.013
Mo–O	3	3.721 ± 0.035	0.013
Mo–O	3	3.887 ± 0.040	0.013
Mo–O	6	4.154 ± 0.022	0.012
Mo–O	3	4.441 ± 0.058	0.012
Mo–O	3	4.637 ± 0.068	0.012

$\Delta E_0=0$ ,  $N_{\text{var}}=19$ ,  $N_{\text{ind}}=31$ ,  $R=0.027$ ,  $k\text{-range}=3\text{--}13$ ,  $R\text{-range}=1.000\text{--}6.000$

dealing with incorporation of As<sup>5+</sup> (Bolanz et al. 2013b) and P<sup>5+</sup> (Gálvez et al. 1999) in hematite. Comparable ionic radii of octahedral Fe<sup>3+</sup> (0.65 Å, high-spin state) and Mo<sup>6+</sup> (0.59 Å) (Shannon 1979) suggest that Mo<sup>6+</sup> could substitute for Fe<sup>3+</sup> in a crystal structure. Systematic changes of the cell parameters and the absence of impurities support this assumption.

The XANES spectra at the Mo *L*<sub>3</sub>-edge are sensitive indicators for the Mo coordination in various structures (Bare et al. 1993; Aritani et al. 1996). The ligand field splitting of the 4d orbitals causes characteristic splitting of the white line (Hedman et al. 1984). The split white line is attributed to the electron transition from 2p<sub>3/2</sub> to split 4d states, i.e. t<sub>2</sub> (d<sub>xy</sub>, d<sub>xz</sub>, d<sub>yz</sub>) and e (d<sub>x<sup>2</sup>-y<sup>2</sup></sub>, d<sub>z<sup>2</sup></sub>) (Aritani et al. 1996). According to ligand-field theory, for tetrahedral coordination, the intensity of the first peak should be lower than the second (e:t<sub>2</sub>=2:3) and vice versa for octahedral coordination (t<sub>2g</sub>:e<sub>g</sub>=3:2) (Bare et al. 1993). Typical peak-splitting values for tetrahedral compounds lie between 1.8 and 2.4 eV, whereas octahedral values are greater at 3.1–4.5 eV (Bare et al. 1993). Values of 3.21–3.27 eV for the peak splitting of hematite, therefore, could be attributed to the incorporation of a distorted MoO<sub>6</sub> octahedron (Aritani et al. 1996).

Replacing one Fe<sup>3+</sup> of a hematite supercell by Mo<sup>6+</sup> and subsequent fitting of this structure supported the formation of a distorted MoO<sub>6</sub> octahedron (for Mo–O distances see Table 8) in the first shell. Several factors could contribute to the local distortion of this polyhedron, such as differences in Fe (0.65 Å) and Mo (0.59 Å) ionic radii (Shannon 1979) and the greater electrostatic charge of Mo<sup>6+</sup> compared to Fe<sup>3+</sup>.

The Fe vacancy resulting from the exclusion of the closest face-sharing Fe<sup>3+</sup> atom in this fit enabled the structure

to equilibrate the surplus charge of the incorporated Mo<sup>6+</sup>. The calculations for Fe loss suggested a loss of ~2.10 Fe atoms per Mo atom incorporated (Table 1) and are in good agreement, therefore, with this model and support this valence-balancing process:



The decisive step for Mo incorporation by hematite and goethite seems to be the assimilation of Mo into the poorly crystalline iron oxide, ferrihydrite, where coordination of Mo<sup>6+</sup> changes from tetrahedral to octahedral. Considering that ferrihydrite is a metastable phase which transforms over time to more stable iron oxides, previously incorporated Mo<sup>6+</sup> is then adopted by the newly formed phases. In the next step, ferrihydrite transforms either to hematite by a topotactic solid-state transformation (Cornell and Schwertmann 2003; Cudennec and Lecerf 2006), which is probably why larger amounts of Mo<sup>6+</sup> are incorporated in the structure of hematite than in goethite, or to goethite by a dissolution-reprecipitation process, where significant amounts of the previously bound Mo<sup>6+</sup> are released.

### Goethite

Analyzing the refined data of the goethite pXRD spectra, small but noticeable variation of the unit-cell parameters *a* and *c* with increasing initial Mo:Fe molar ratio (Fig. 4b) were determined. Observations of similar changes for the incorporation of W into goethite by Kreissl et al. (2016) and the analogous behavior of the hematite samples suggested incorporation of Mo<sup>6+</sup> into the crystal structure of the synthesized goethites. No coprecipitated phases were detected in the pXRD spectra. Changes in the chemical composition support this assumption, therefore.

Evaluation of the Mo *K*- and *L*<sub>3</sub>-edge spectra of the synthesized goethites led to only a vague impression of the coordination of Mo in goethite. Peak-splitting values of between 2.60 and 2.82 eV in its *L*<sub>3</sub>-edge XANES spectra were distinctly smaller than for hematite and six-line ferrihydrite. These values are situated between the listed values for tetrahedrally and octahedrally coordinated Mo<sup>6+</sup>. The intensity ratio (~3:2) of the split peaks in its *L*<sub>3</sub>-edge XANES spectrum clearly points to the octahedral coordination of Mo<sup>6+</sup>, however.

In order to resolve the coordination of Mo<sup>6+</sup> in the sample, both tetrahedral as well as octahedral coordination for the fitting of the goethite EXAFS spectra were considered. For tetrahedrally coordinated Mo<sup>6+</sup>, one could assume that the incorporation of the fitted MoO<sub>4</sub><sup>2-</sup> tetrahedron into the used supercell structure in place of an Fe octahedron would greatly distort the goethite structure. Such distortion would be reflected by significant changes in the unit-cell parameters and especially of the unit-cell volume. Given the small amount of Mo in the solids (0.0274 wt.% at the most), only slight changes in the lattice parameters can be observed. The underlying cause of the observed variations in these parameters cannot be stated with certainty. Not only could they stem from the incorporation of Mo in the goethites, but also from the measured particle sizes, from internal

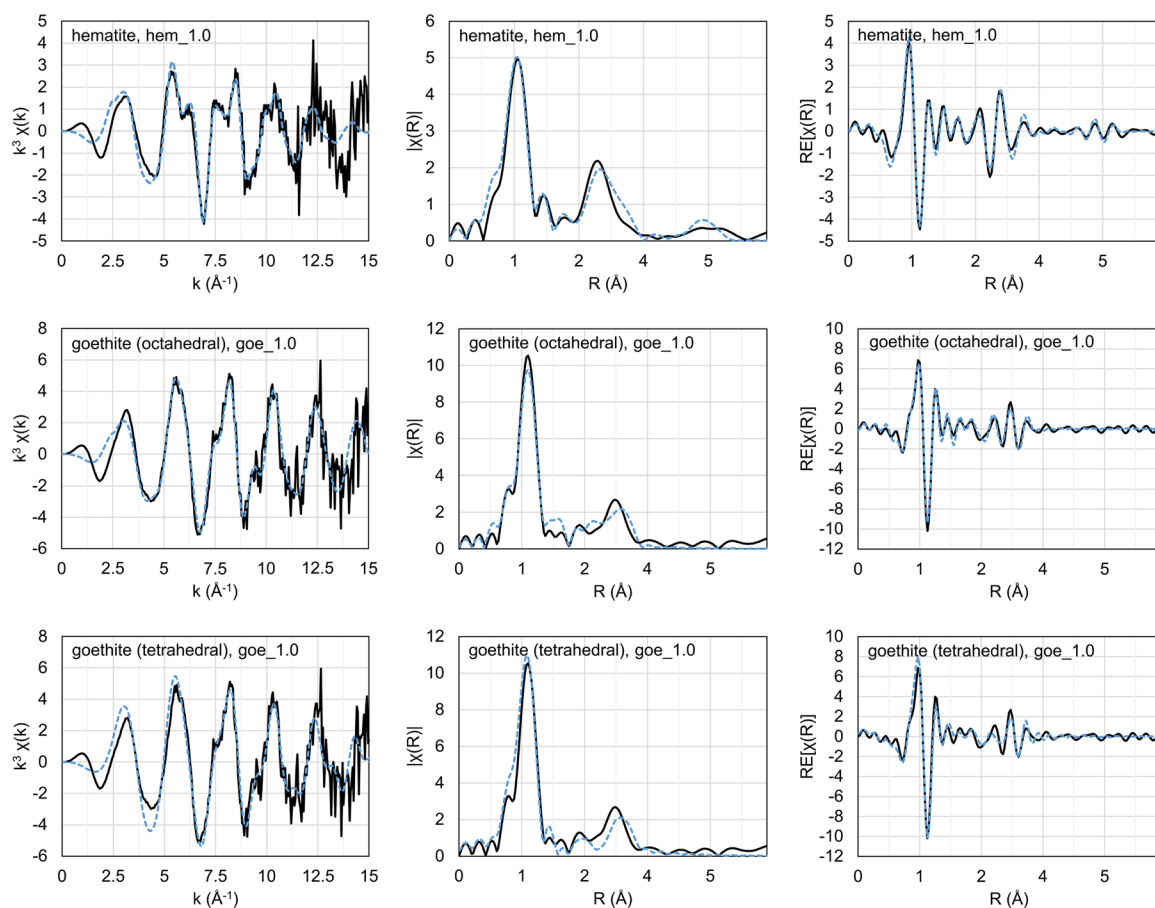


**Fig. 9** Normalized  $k^3$ -weighted Mo  $K$ -edge spectra (left), magnitude of the Fourier transform (middle), and part of the Fourier transform of the Mo  $K$ -edge spectra (right). The thick black lines represent the measured and processed data of hem\_1.0 and goe\_1.0, the dashed blue lines represent the fits. All spectra are uncorrected for phase shift

strain of the probes, and from adsorbed ions. The observed changes in the lattice parameters could, at most, serve as a possible hint that no  $\text{MoO}_4^{2-}$  tetrahedra were incorporated, therefore.

To pursue the approach of tetrahedrally coordinated Mo, the adsorption of tetrahedrally coordinated  $\text{MoO}_4^{2-}$  on the surface of goethite was assumed. The fitting resulted in a model where  $\text{MoO}_4^{2-}$  tetrahedra were adsorbed as

**Table 5** Scattering paths for tetrahedrally coordinated  $\text{MoO}_4^{2-}$  adsorbed on goethite (goe\_1.0)

Single scattering paths	$N$	$d$ (Å)	$\sigma^2$
Mo–O	4	$1.780 \pm 0.002$	0.004
Mo–Fe	1	$2.895 \pm 0.035$	0.012
Mo–Fe	1	$3.578 \pm 0.019$	0.002

$\Delta E_0=0$ ,  $N_{\text{var}}=8$ ,  $N_{\text{ind}}=36$ ,  $R=0.079$ ,  $k$ -range=2.5–14.0,  $R$ -range=1.000–6.000

inner-sphere complexes on the goethite surface. Adsorption would explain the split second-shell feature between 2.2 and 3.4 Å (not corrected for phase shift) in the EXAFS

**Table 6.** Scattering paths for octahedrally coordinated  $\text{Mo}^{6+}$  in goethite (goe\_1.0)

Single scattering paths	$N$	$d$ (Å)	$\sigma^2$
Mo–O	1	$1.783 \pm 0.005$	0.003
Mo–O	2	$1.785 \pm 0.002$	0.003
Mo–O	1	$2.002 \pm 0.019$	0.003
Mo–O	1	$2.160 \pm 0.019$	0.003
Mo–O	1	$2.291 \pm 0.018$	0.003
Mo–Fe	1	$2.926 \pm 0.023$	0.011
Mo–O	1	$3.209 \pm 0.067$	0.011
Mo–Fe	2	$3.316 \pm 0.025$	0.011
Mo–Fe	4	$3.594 \pm 0.010$	0.011

$\Delta E_0=0$ ,  $N_{\text{var}}=13$ ,  $N_{\text{ind}}=36$ ,  $R=0.036$ ,  $k$ -range=2.5–14.0,  $R$ -range=1.000–6.000

**Table 7.** Interatomic distances of Mo<sup>6+</sup> and O<sup>2-</sup> ( $d_{\text{Mo-O}}$ ) in selected oxysalts of molybdenum

Sample	$d_{\text{Mo-O}}$ (Å)
CaMoO <sub>4</sub> (Hazen et al. 1985)	1.771
CdMoO <sub>4</sub> (Daturi et al. 1997)	1.751
FeMoO <sub>4</sub> (Rapposch et al. 1980)	1.633–1.780
FeVMoO <sub>7</sub> (Le Bail et al. 1995)	1.631–1.741
Na <sub>2</sub> MoO <sub>4</sub> (Fortes 2015)	1.772
K <sub>2</sub> MoO <sub>4</sub> (Gatehouse and Leverett 1969)	1.742–1.785
(NH <sub>4</sub> ) <sub>8</sub> Mo <sub>10</sub> O <sub>34</sub> (Benchrifra and de Pape 1990)	1.701–1.867

spectrum of goethite (Fig. 9) fairly well. The first peak of this feature between 2.2 and 2.5 Å (not corrected for phase shift) could be explained by an edge-sharing complex via bidentate mono-nuclear linkage. The second, more intense peak (2.7–3.4 Å) could be explained by corner-sharing, inner-sphere surface complexes bound by monodentate mononuclear linkage. The Mo–Fe distances for both complexes, 2.90(4) Å for the bidentate one and 3.58(2) Å for the monodentate complex, were in good agreement with the values suggested by Arai (2010), ~2.81 Å for edge-sharing bidentate Mo–Fe complexes, as well as ~3.59 Å for As–Fe and ~3.63 Å for Cr–Fe linkages postulated by Fendorf et al. (1997).

As expected, considering the peak-splitting values of the Mo  $L_3$ -edge XANES spectrum of goethite, fitting of the structure where one Fe<sup>3+</sup> of the goethite supercell is replaced by Mo<sup>6+</sup>, results in the formation of a strongly distorted MoO<sub>6</sub> octahedron (for Mo–O distances see Table 6) in the first shell. Three positive excess charges created by the substitution of Fe<sup>3+</sup> by Mo<sup>6+</sup> must be compensated. One possible way to compensate the excess charge would be the

**Table 8.** Scattering paths for octahedrally coordinated Mo<sup>6+</sup> in hematite (hem\_1.0)

Single scattering paths	$N$	$d$ (Å)	$\sigma^2$
Mo–O	1	2.308 ± 0.017	0.007
Mo–O	2	2.067 ± 0.006	0.007
Mo–O	3	1.790 ± 0.003	0.007
Mo–Fe	3	3.169 ± 0.008	0.014
Mo–Fe	3	3.412 ± 0.009	0.014
Mo–Fe	6	3.589 ± 0.010	0.014
Mo–Fe	1	3.794 ± 0.040	0.014
Mo–Fe	3	4.995 ± 0.023	0.012
Mo–Fe	3	5.134 ± 0.027	0.012
Mo–Fe	6	5.303 ± 0.016	0.012

$\Delta E_0 = 0$ ,  $N_{\text{var}} = 15$ ,  $N_{\text{ind}} = 24$ ,  $R = 0.027$ ,  $k\text{-range} = 2.5\text{--}12$ ,  $R\text{-range} = 1.000\text{--}5.000$

release of three H<sup>+</sup> atoms. This could lead to a significant reduction of the hydrogen content in goethite, especially for greater Mo concentrations. This deprotonation mechanism was shown by Bolanz et al. (2013b) to work for low concentrations of highly charged ions such as Sb<sup>3+</sup> only. If the concentration of such ions increases, the goethite structure would probably collapse due to missing hydrogen bonds. In dehydroxylation experiments, the break-down of the goethite structure was shown by Gualtieri and Venturelli (1999) to have occurred long before the depletion of the hydroxyl groups. Based on spectroscopic analyses, the formation of Fe<sup>3+</sup> vacancies as previously assumed for Mo-bearing hematite seems to be the more likely charge-balancing reaction. This would reduce the four edge-sharing Fe octahedra related to the Mo octahedron incorporated to just three and further improve the goodness of the fit.

As seen by comparing the results of this model with those in which tetrahedral MoO<sub>4</sub><sup>2-</sup> was adsorbed to goethite, the fit of octahedrally coordinated Mo is in better agreement with the measured EXAFS spectrum of goe\_1.0. This model goes much better with the observations of the pXRD measurements. Incorporation of the distorted MoO<sub>6</sub> octahedron caused the structural disorder of the synthesized goethites to increase and explains the observed alteration of the cell parameters, therefore (Table 1, Fig. 4b) (Cornell and Schwertmann 2003). No additional phases containing MoO<sub>4</sub><sup>2-</sup> were observed in the pXRD spectra.

## SUMMARY AND CONCLUSIONS

Iron oxides hematite, six-line ferrihydrite, and goethite have the ability to control the bioavailability of micro-nutrients such as Mo and contaminants in soils (Cornell and Schwertmann 2003). Their large adsorption capacities for trace elements in solutions (Peacock and Sherman 2004; Rout et al. 2012) but also for element uptake via coprecipitation (Martínez and McBride 1998, 2001; Manceau et al. 2000) make them well known scavengers for metals and metalloids (e.g. Sieber et al. 1985; Dardenne et al. 2002). Although surface adsorption might play a significant role in short-term retention of such substances, previous studies proposed that structural incorporation might likewise be an important process to contain these substances but for prolonged periods.

Based on chemical and spectroscopic data presented in the current study, the incorporation mechanisms of Mo<sup>6+</sup> in the structure of the most common iron oxide phases (i.e. hematite, six-line ferrihydrite, and goethite) were investigated.

Clear indications for changes in the structure of the investigated iron phases are provided by significantly correlated changes for the unit-cell parameters of hematite and goethite with increasing Mo contents. XANES measurements at the Mo  $L_3$ -edge sustain the structural incorporation of Mo<sup>6+</sup> in the structure of all three phases. The splitting of the white line suggests the transformation of the originally tetrahedrally

coordinated  $\text{Mo}^{6+}$  in  $\text{Na}_2\text{MoO}_4 \cdot 2\text{H}_2\text{O}$  which was used for the synthesis to octahedrally coordinated  $\text{Mo}^{6+}$  in the iron oxide phases obtained. Fitting of the EXAFS spectra with structural models of hematite, ferrihydrite, and goethite, with Mo residing in the Fe position, led to reasonable Mo–O distances which matched a strongly distorted  $\text{MoO}_6$  octahedron incorporated in the structure of all three phases and excluded theoretical models of  $\text{MoO}_4^{2-}$  tetrahedra adsorbed on the surface of goethite or incorporated in the crystal structures of ferrihydrite and goethite.

These findings support the structural incorporation of  $\text{Mo}^{6+}$  in hematite, six-line ferrihydrite, and goethite by heterovalent substitution of one octahedrally coordinated  $\text{Fe}^{3+}$  by  $\text{Mo}^{6+}$ . In the case of hematite and goethite, this substitution led to the formation of an additional  $\text{Fe}^{3+}$  vacancy, which compensated the three surplus charges.

Characterizing the incorporation mechanisms of  $\text{Mo}^{6+}$  into the crystal structure of six-line ferrihydrite, goethite, and hematite, some of the most common iron oxides, improves understanding of its long-time retention in soils and may represent a long-term control on Mo, as well as other similar metalloids with high coordination numbers in environmental settings. This is relevant to a number of systems, including mining environments, where potentially hazardous metals can be released to the surrounding ecosystem, and agricultural areas, where the bioavailability of  $\text{MoO}_4^{2-}$  affects the growth of crops and the health of grazing ruminants. In general, the retention of  $\text{Mo}^{6+}$  by incorporation into iron oxides makes  $\text{MoO}_4^{2-}$  less bioavailable for plants and microorganisms (Lang and Kaupenjohann 1999), therefore affecting the global nitrogen cycle, as nitrogen fixation and nitrate assimilation can be restricted.

One of the most environmentally consequential polyvalent metals is uranium. Its importance arises as it is the most significant radioactive radionuclide by mass of all environmental contaminants. Because of its long half-life (4.5 Ga), its behavior, and its decay chain, studies dealing with the limitation of uranium migration and its long-term retention are of great environmental importance. In particular, uranium could be incorporated into hematite during ferrihydrite aggregation and the early stages of crystallization, according to Marshall et al. (2014). The XAS data by those authors indicated the incorporation of  $\text{U}^{6+}$  into a distorted octahedral coordination replacing  $\text{Fe}^{3+}$ . Atomistic simulations by Kerisit et al. (2011, 2016) support these findings. The replacement of  $\text{Fe}^{3+}$  by  $\text{U}^{6+}$  in greatly distorted octahedral coordination bears considerable resemblance to the behavior of  $\text{Mo}^{6+}$  as seen in the present study. As no suitable charge-compensation mechanism within the constraints of the EXAFS measurements of Marshall et al. (2014) could be identified, the possibility exists that  $\text{U}^{6+}$  follows not only the same incorporation mechanism but also the same charge-compensation mechanism as  $\text{Mo}^{6+}$  during its incorporation into hematite. Additional simulations (Kerisit et al. 2011, 2016) support the octahedral incorporation of  $\text{U}^{6+}$  in place of  $\text{Fe}^{3+}$  in goethite, with the result that one can assume that

both  $\text{Mo}^{6+}$  and  $\text{U}^{6+}$  incorporation into hematite and goethite are subjected to the same mechanisms.

Incorporation of Mo in various iron oxides can be considered, therefore, as a reasonable indication of the uranium scavenger behavior of such minerals; in order to confirm this hypothesis, more comparative analyses are needed. If this assumption proves to be true, molybdenum can be used as a safe surrogate for uranium in some experiments concerning its migration in natural engineered environments as well as for long-term immobilization.

## ACKNOWLEDGMENTS

Open Access funding has been enabled and organized by Projekt DEAL, (Germany). The authors thank Dirk Merten and Ines Kamp (Friedrich-Schiller-University Jena) for their support during the ICP-OES analyses. They are grateful to the Karlsruhe Institute of Technology for the beamtime on the SUL-X beamline at the Karlsruhe Research Accelerator (KARA) and acknowledge the Diamond Light Source for time on beamline B18 under proposal SP13606. The Friedrich-Schiller-University, Germany, where most of the experiments were conducted, is also acknowledged. This project was funded by the Deutsche Forschungsgemeinschaft (DFG) through project BO 4534/4-1.

### Funding

Funding sources are as stated in the Acknowledgments.

### Declarations

### Conflict of Interest

The authors declare that they have no conflict of interest.

**Open Access** This article is licensed under a Creative Commons Attribution 4.0 International License, which permits use, sharing, adaptation, distribution and reproduction in any medium or format, as long as you give appropriate credit to the original author(s) and the source, provide a link to the Creative Commons licence, and indicate if changes were made. The images or other third party material in this article are included in the article's Creative Commons licence, unless indicated otherwise in a credit line to the material. If material is not included in the article's Creative Commons licence and your intended use is not permitted by statutory regulation or exceeds the permitted use, you will need to obtain permission directly from the copyright holder. To view a copy of this licence, visit <http://creativecommons.org/licenses/by/4.0/>.

## REFERENCES

- Arai, Y. (2010). X-ray absorption spectroscopic investigation of molybdenum multinuclear sorption mechanism at the goethite-water interface. *Environmental Science & Technology*, 44, 8491–8496.
- Aritani, H., Tanaka, T., Funabiki, T., & Yoshida, S. (1996). Study of the local structure of molybdenum-magnesium binary oxides by means of Mo L3-edge XANES and

- UV-Vis spectroscopy. *Journal of Physical Chemistry*, *100*, 19495–19501.
- Balko, B. A., & Clarkson, K. M. (2001). The effect of doping with Ti(IV) and Sn(IV) on oxygen reduction at hematite electrodes. *Journal of the Electrochemical Society*, *148*, E85–E91.
- Bare, S. R., Mitchell, G. E., Maj, J. J., Edwin, G., Vrieland, E., & Gland, J. L. (1993). Local site symmetry of dispersed molybdenum oxide catalysts: XANES at the Mo L<sub>2,3</sub>-edges. *Journal of Physical Chemistry*, *97*, 6048–6053.
- Barron, A. R., Wurzbarger, N., Bellenger, J. P., Wright, S. J., Kraepiel, A. M. L., & Hedin, L. O. (2009). Molybdenum limitation of asymbiotic nitrogen fixation in tropical forest soils. *Nature Geoscience*, *2*, 42–49.
- Benchrif, R., & Pape, R. (1990). Isotopism of the triclinic Ti<sub>8</sub>Mo<sub>10</sub>O<sub>34</sub> and (NH<sub>4</sub>)<sub>8</sub>Mo<sub>10</sub>O<sub>34</sub> molybdates. *Acta Crystallographica Section C*, *46*, 728–728.
- Blake, R. L., Hesseveick, R. E., Zoltai, T., & Finger, L. W. (1966). Refinement of the hematite structure. *American Mineralogist*, *51*, 123–129.
- Bolanz, R. M., Wierzbicka-Wieczorek, M., Čaplovičová, M., Uhlík, P., Göttlicher, J., Steininger, R., & Majzlan, J. (2013a). Structural incorporation of As<sup>5+</sup> into hematite. *Environmental Science & Technology*, *47*, 9140–9147.
- Bolanz, R. M., Bläss, U., Ackermann, S., & Ciobotă, V., Rösch, P., Tarcea, N., Popp, J., and Majzlan, J. (2013b). The effect of antimonate, arsenate, and phosphate on the transformation of ferrihydrite to goethite, hematite, ferrioxhyte, and triphuyite. *Clays and Clay Minerals*, *61*, 11–25.
- Bolanz, R. M., Grauer, C., Cooper, R. E., Göttlicher, J., Steininger, R., Perry, S., & Küsel, K. (2017). Incorporation of molybdenum(VI) in akaganéite (β-FeOOH) and the microbial reduction of Mo-akaganéite by *Shewanella loihica* PV-4. *CrystEngComm*, *19*, 6189–6198.
- Bortels, H. (1930). Molybdän als Katalysator bei der biologischen Stickstoffbindung. *Archives of Microbiology*, *1*, 333–342.
- Brinza, L., Benning, L. G., & Stham, P. J. (2008). Adsorption studies of Mo and V onto ferrihydrite. *Mineralogical Magazine*, *72*, 385–388.
- Brinza, L., Vu, H. P., Shaw, S., Mosselmans, J. F. W., & Benning, L. G. (2015). Effect of Mo and V on the hydrothermal crystallization of hematite from ferrihydrite: an in situ energy dispersive X-ray diffraction and X-ray absorption spectroscopy study. *Crystal Growth & Design*, *15*, 4768–4780.
- Carroll, D., & Richmond, W. R. (2008). Incorporation of molybdate anion into □-FeOOH. *American Mineralogist*, *93*, 1641–1646.
- Ciobanu, C. L., Wade, B. P., Cook, N. J., Schmidt Mumm, A., & Giles, D. (2013). Uranium-bearing hematite from the Olympic Dam Cu–U–Au deposit, South Australia: A geochemical tracer and reconnaissance Pb–Pb geochronometer. *Precambrian Research*, *238*, 129–147.
- Cornell, R. M., & Giovanoli, R. (1987). Effect of manganese on the transformation of ferrihydrite into goethite and jacobsite in alkaline media. *Clays and Clay Minerals*, *35*, 11–20.
- Cornell, R. M., & Schwertmann, U. (2003). *The Iron Oxides, Properties, Reactions, Occurrences, and Uses*. Wiley-VCH Verlag, Hoboken, New Jersey, USA.
- Cudennec, Y., & Lecerf, A. (2006). The transformation of ferrihydrite into goethite or hematite, revisited. *Journal of Solid State Chemistry*, *179*, 716–722.
- Dardenne, K., Schäfer, T., Lindqvist-Reis, P., Denecke, M. A., Plaschke, M., Rothe, J., & Kim, J. I. (2002). Low temperature XAFS investigation on the lutetium binding changes during the 2-line ferrihydrite alteration process. *Environmental Science & Technology*, *36*(23), 5092–5099.
- Das, S., Essilfie-Dughan, J., & Hendry, M. J. (2016). Sequestration of molybdate during transformation of 2-line ferrihydrite under alkaline conditions. *Applied Geochemistry*, *73*, 70–80.
- Daturi, M., Busca, G., Borel, M. M., Leclaire, A., & Piaggio, P. (1997). Vibrational and XRD study of the system CdWO<sub>4</sub>-CdMoO<sub>4</sub>. *Journal of Physical Chemistry*, *101*, 4358–4369.
- De Leon, M. J., Rehr, J. J., Zabinsky, S. I., & Albers, R. C. (1991). Ab initio curved-wave X-ray-absorption fine structure. *Physical Review*, *44*, 4146–4156.
- Fendorf, S. E., Eick, M. J., Gossli, P. R., & Sparks, D. L. (1997). Arsenate and chromate retention mechanisms on goethite. I. Surface structure. *Environmental Science & Technology*, *31*, 315–320.
- Fortes, A. D. (2015). Crystal structures of spinel-type Na<sub>2</sub>MoO<sub>4</sub> and Na<sub>2</sub>WO<sub>4</sub> revisited using neutron powder diffraction. *Acta Crystallographica E*, *71*, 592–596.
- Gálvez, N., Barron, V., & Torrent, J. (1999). Effect of phosphate on the crystallization of hematite, goethite, and lepidocrocite from ferrihydrite. *Clays and Clay Minerals*, *47*, 304–311.
- Gatehouse, B.M. & Leverett, P. (1969). Crystal structure of potassium molybdate, K<sub>2</sub>MoO<sub>4</sub>. *Journal of the Chemical Society A*, 849–854.
- Goldberg, S., Forster, H. S., & Godfrey, C. L. (1996). Molybdenum adsorption on oxides, clay minerals, and soils. *Soil Science Society of America Journal*, *60*(2), 425–432.
- Gualtieri, A., & Venturelli, P. (1999). In situ study of the goethite-hematite phase transformation by real time synchrotron powder diffraction. *American Mineralogist*, *84*, 895–904.
- Hazen, R. M., Finger, L. W., & Mariathasan, J. W. E. (1985). High-pressure crystal chemistry of scheelite-type tungstates and molybdates. *Journal of Physics and Chemistry of Solids*, *46*, 253–263.
- He, Z. L. L., Yang, X. E., & Stoffella, P. J. (2005). Trace elements in agroecosystems and impacts on the environment. *Journal of Trace Elements in Medicine and Biology*, *19*, 125–140.
- Hedman B., Penner-Hahn J.E. & Hodgson K.O. (1984). Molybdenum LII,III edge studies. In Hodgson K.O., Hedman B. & Penner-Hahn J.E. (eds), EXAFS and Near Edge Structure III. Springer Proceedings in Physics, 2 (pp. 64–66).
- Hochella, M. F., Kasama, T., Putnis, A., Putnis, C. V., & Moore, J. N. (2005). Environmentally important, poorly crystalline Fe/Mn hydrous oxides: Ferrihydrite and a possibly new vernadite-like mineral from the Clark Fork River Superfund Complex. *American Mineralogist*, *90*, 718–724.
- Jansen, E., Kyek, A., Schafer, W., & Schwertmann, U. (2002). The structure of six-line ferrihydrite. *Applied Physics A*, *74*, S1004–S1006.
- Kerisit, S., Felmy, A. R., & Ilton, E. S. (2011). Atomistic simulations of uranium incorporation in the structure of hematite. *Environmental Science & Technology*, *45*, 2770–2776.
- Kerisit, S., Bylaska, E. J., Massey, M. S., McBriarty, M. E., & Ilton, E. S. (2016). Ab initio molecular dynamics of uranium incorporated in goethite (□-FeOOH): Interpretation of X-ray absorption spectroscopy of trace polyvalent metals. *Inorganic Chemistry*, *55*, 11736–11746.
- Khan, A., Chen, P., Boolchand, P., & Smirniotis, P. G. (2008). Modified nano-crystalline ferrites for high-temperature WGS membrane reactor applications. *Journal of Catalysis*, *253*, 91–104.
- Klementiev, K.V. (2012). XAFSmass, A program for calculating the mass of XAFS samples. <http://www.cells.es>

- [Beamlines/CLAESS/software/ xafsmass.html](#). Accessed December 2017.
- Kreissl, S., Bolanz, R., Göttlicher, J., Steininger, R., Tarassov, M., & Markl, G. (2016). Structural incorporation of  $W^{6+}$  into hematite and goethite: A combined study of natural and synthetic iron oxides developed from precursor ferrihydrite and the preservation of ancient fluid compositions in hematite. *American Mineralogist*, *101*, 2701–2715.
- Lang, F. (2000). Molybdän-Mobilität und -Mobilisierbarkeit auf sauren Waldstandorten: Prozesse und Einflussfaktoren. Hohenheimer Bodenkundliche Hefte, 57.
- Lang, F., & Kaupenjohann, M. (1999). Molybdenum fractions and mobilization kinetics in acid forest soils. *Journal of Plant Nutrition and Soil Science*, *162*, 309–314.
- Le Bail, A., Permer, L., & Laligant, Y. (1995). Structure of  $FeVMoO_7$ . *European Journal of Solid State and Inorganic Chemistry*, *32*, 883–892.
- Liang, L., & Zhu, J.-M. (2016). An optimized sequential extraction scheme for molybdenum association in environmental samples. *Acta Geochimica*, *35*, 111–119.
- Linehan, J. C., Darab, J. G., Matson, D. W., Chen, X., & Amonette, J. E. (1997). Synthesis and characterization of akaganéite-like ferric oxyhydroxides. *Materials Research Society Symposium Proceedings*, *432*, 157–161.
- Manceau, A., Schlegel, M. L., Musso, M., Sole, V. A., Gauthier, C., Petit, P. E., & Trolard, F. (2000). Crystal chemistry of trace elements in natural and synthetic goethite. *Geochimica et Cosmochimica Acta*, *64*(21), 3643–3661.
- Marshall, T. A., Morris, K., Law, G. T. W., Livens, F. R., Mosselmans, J. F. W., Bots, P., & Shaw, S. (2014). Incorporation of uranium into hematite during crystallization from ferrihydrite. *Environmental Science & Technology*, *48*, 3724–3731.
- Martínez, C. E., & McBride, M. B. (1998). Solubility of  $Cd^{2+}$ ,  $Cu^{2+}$ ,  $Pb^{2+}$ , and  $Zn^{2+}$  in aged coprecipitates with amorphous iron hydroxides. *Environmental Science & Technology*, *32*, 743–748.
- Martínez, C. E., & McBride, M. B. (2001). Cd, Cu, Pb, and Zn coprecipitates in Fe oxide formed at different pH: Aging effects on metal solubility and extractability by citrate. *Environmental Toxicology and Chemistry*, *20*, 122–126.
- Mendel, R. R., & Bittner, F. (2006). Cell biology of molybdenum. *Biochimica et Biophysica Acta*, *1763*, 621–635.
- Michel, F. M., Ehm, L., Antao, S. M., Lee, P. L., Chupas, P. J., Liu, G., Strongin, D. R., Schoonen, M. A. A., Phillips, B. L., & Parise, J. B. (2007). The structure of ferrihydrite, a nanocrystalline material. *Science*, *316*, 1726–1729.
- Mullet, M., Demousson, F., Humbert, B., Michot, L. J., & Vantelon, D. (2007). Aqueous Cr(VI) reduction by pyrite: Speciation and characterization of the solid phases by X-ray photoelectron, Raman and X-ray absorption spectroscopies. *Geochimica et Cosmochimica Acta*, *71*(13), 3257–3271.
- Neunhäuser, C., Berreck, M., & Insam, H. (2001). Remediation of soils contaminated with molybdenum using soil amendments and phytoremediation. *Water, Air, & Soil Pollution*, *128*, 85–96.
- Norrish, K. (1975). Geochemistry and mineralogy of trace elements. In Nicholas, A.R. & Egan, D.J. (eds.), *Trace Elements in Soil-Plant-Animal Systems* (pp. 55–81). Academic Press, New York.
- Orlandi, P., Pasero, M., & Bigi, S. (2010). Sardignaitite, a new mineral, the second known bismuth molybdate: Description and crystal structure. *Mineralogy and Petrology*, *100*, 17–22.
- Peacock, C. L., & Sherman, D. M. (2004). Vanadium (V) Adsorption onto goethite ( $\alpha$ -FeOOH) at pH 1.5 to 12: a surface complexation model based on ab initio molecular geometries and EXAFS spectroscopy. *Geochimica et Cosmochimica Acta*, *68*, 1723–1733.
- Petříček, V., Dušek, M., & Palatinus, L. (2014). Crystallographic Computing System JANA2006. *Zeitschrift für Kristallographie*, *229*(5), 345–352.
- Post, J. E., Heaney, P. J., Von Dreele, R. B., & Hanson, J. C. (2003). Neutron and temperature-resolved synchrotron X-ray powder diffraction study of akaganéite. *American Mineralogist*, *88*, 782–788.
- Rapposch, M. H., Anderson, J. B., & Kostiner, E. (1980). Crystal structure of ferric molybdate,  $Fe_2(MoO_4)_3$ . *Inorganic Chemistry*, *19*, 3531–3539.
- Ravel, B., & Newville, M. (2005). Athena, artemis, hephaestus: data analysis for X-ray absorption spectroscopy using IFEFIT. *Journal of Synchrotron Radiation*, *12*, 537–541.
- Richmond, W. R., Hockridge, J. G., Loan, M., & Parkinson, G. M. (2004). A new iron oxyhydroxide phase: The molybdate-substituted analogue of akaganéite. *Chemistry of Materials*, *16*, 3203–3205.
- Rout, K., Mohapatra, M., & Anand, S. (2012). 2-line ferrihydrite: Synthesis, characterization and its adsorption behavior for removal of Pb(II), Cd(II), Cu(II) and Zn(II) from aqueous solutions. *Dalton Transactions*, *41*, 3302–3312.
- Scheinost, A. C., Rossberg, A., Vantelon, D., Xifra, I., Kretzschmar, R., Leuz, A. K., & Johnson, C. A. (2006). Quantitative antimony speciation in shooting-range soils by EXAFS spectroscopy. *Geochimica et Cosmochimica Acta*, *70*, 3299–3312.
- Schwertmann, U. & Cornell, R.M. (2000). Iron oxides in the laboratory: Preparation and characterization. Wiley-VCH Verlag, Weinheim, 2nd edn.
- Shannon, R. D. (1979). Revised effective ionic radii and systematic studies of interatomic distances in halides and chalcogenides. *Acta Crystallographica*, *32*, 751–767.
- Sherman, D. M., & Randall, S. R. (2003). Surface complexation of arsenic(V) to iron(III) (hydr)oxides: Structural mechanism from ab initio molecular geometries and EXAFS spectroscopy. *Geochimica et Cosmochimica Acta*, *67*, 4223–4230.
- Sieber, K. D., Sanchez, C., Turner, J. E., & Somorjai, G. A. (1985). Preparation, electrical and photoelectrochemical properties of magnesium doped iron oxide sintered discs. *Materials Research Bulletin*, *20*, 153–162.
- Stiefel, E. L. (2002). The biogeochemistry of molybdenum and tungsten. *Metal Ions in Biological Systems*, *39*, 1–29.
- Tarassov, M., Mihailova, B., Tarassova, E., & Konstantinov, L. (2002). Chemical composition and vibrational spectra of tungsten-bearing goethite and hematite from Western Rhodopes, Bulgaria. *European Journal of Mineralogy*, *14*, 977–986.
- Vu, H. P., Shaw, S., Brinza, L., & Benning, L. G. (2010). Crystallization of hematite ( $\alpha$ - $Fe_2O_3$ ) under alkaline condition: The effects of Pb. *Crystal Growth & Design*, *10*, 1544–1551.
- Wang, D., Aller, R. C., & Sañudo-Wilhelmy, S. A. (2011). Redox speciation and early diagenetic behavior of dissolved molybdenum in sulfidic muds. *Marine Chemistry*, *125*, 101–107.



Wells, M. A., Gilkes, R. J., & Fitzpatrick, R. W. (2001). Properties and acid dissolution of metal-substituted hematites. *Clays and Clay Minerals*, 49, 60–72.

Williams, R. J. P., & Frausto da Silva, J. J. R. (2002). The involvement of molybdenum in life. *Biochemical and Biophysical Research Communications*, 292, 293–299.

Žemberyová, M., Hagarová, I., Zimová, J., Barteková, J., & Kuss, H.-M. (2010). Determination of molybdenum in extracts of

soil and sewage sludge CRMs after fractionation by means of BCR modified sequential extraction procedure. *Talanta*, 82, 582–586.

(Received 14 October 2020; revised 12 February 2021; AE: Yuji Arai)